NANO LETTERS

August 21, 2024
Volume 24, Number 33
pubs.acs.org/NanoLett

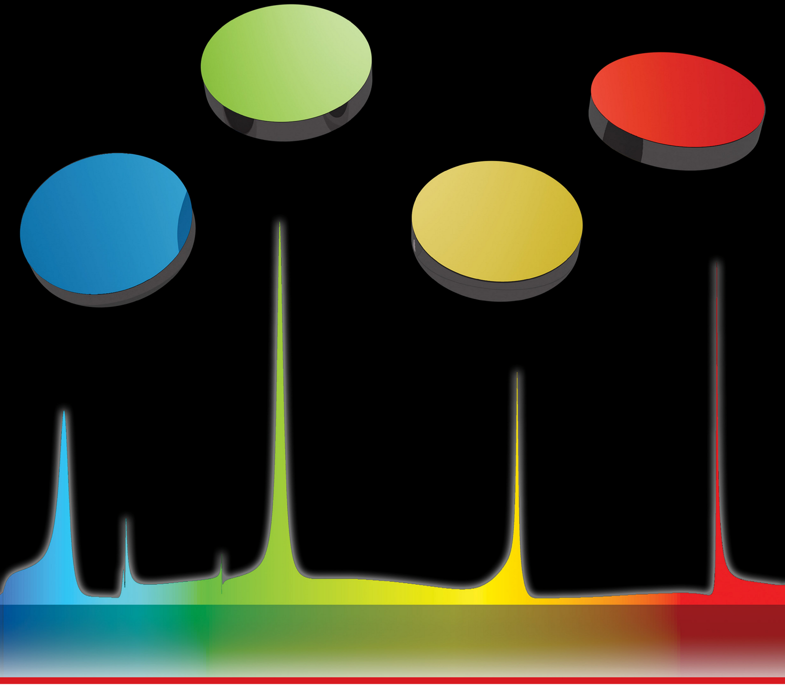

ACS Publications
Most Trusted. Most Cited. Most Read.

www.acs.org

NANO LETTERS

Open Access

pubs.acs.org/NanoLett

Letter

# Topology Optimization Enables High-*Q* Metasurface for Color Selectivity

Huan-Teng Su, Lu-Yun Wang, Chih-Yao Hsu, Yun-Chien Wu, Chang-Yi Lin, Shu-Ming Chang, and Yao-Wei Huang*

**Cite This:** *Nano Lett.* 2024, 24, 10055−10061

Read Online

ACCESS | Metrics & More | Article Recommendations | Supporting Information

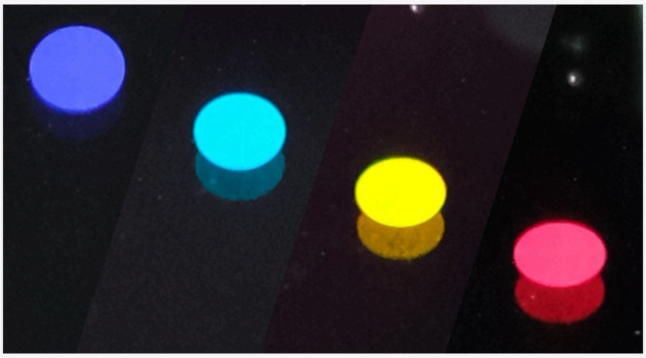

**ABSTRACT:** Nonlocal metasurfaces, exemplified by resonant waveguide gratings (RWGs), spatially and angularly configure optical wavefronts through narrow-band resonant modes, unlike the broad-band and broad-angle responses of local metasurfaces. However, forward design techniques for RWGs remain constrained at lower efficiency. Here, we present a topology-optimized metasurface resonant waveguide grating (MRWG) composed of titanium dioxide on a glass substrate capable of operating simultaneously at red, yellow, green, and blue wavelengths. Through adjoint-based topology optimization, while considering nonlocal effects, we significantly enhance its diffraction efficiency, achieving numerical efficiencies up to 78% and *Q*-factors as high as 1362. Experimentally, we demonstrated efficiencies of up to 59% with a *Q*-factor of 93. Additionally, we applied our topology-optimized metasurface to color selectivity, producing vivid colors at 4 narrow-band wavelengths. Our investigation represents a significant advancement in metasurface technology, with potential applications in see-through optical combiners and augmented reality platforms.

**KEYWORDS:** *metasurfaces, nonlocal, color selection, gratings, topology optimization*

Metasurfaces are categorized into local and nonlocal based on their characteristics and behavior of building blocks.[1,2] In the realm of metasurfaces, local and nonlocal variants exhibit distinct characteristics. Local metasurfaces shape the phase of incident light by referencing precomputed optical responses,[3−5] which provides intuitive and convenient forward design of optics, such as metalenses,[6] metasurface holograms,[7−9] vortex lasers,[10] etc. However, these devices often encounter limitations in spectral control. Due to the confinement of optical interactions within deeply subwavelength structures, they tend to exhibit broad-band characteristics, resulting in wavefront deformation across a wide frequency range. In contrast, nonlocal metasurfaces, such as guided-mode resonance gratings (RWGs),[11−13] quasi-bound states in the continuum (q-BIC) structures,[14−16] and perturbative structures,[17,18] yield sharp spectral features. This is because guided-mode resonance gratings approximate the pure slab waveguide, enabling the excitation of multiple modes simultaneously at different wavelengths and resulting in higher quality factors (*Q*-factor). Additionally, q-BIC structures break the in-plane inversion symmetry through perturbations, leading to the creation of q-BIC with high yet finite *Q*-factors. However, traditional forward design approaches for RWGs and q-BIC structures often exhibit lower efficiency.[12,15]

RWGs defined based on their physical behavior rely on guided modes propagating over multiple gratings with geometrical continuity. RWGs consist of a waveguide and a dielectric grating. Due to the interaction between these two components, the exit spectrum exhibits many unique optical properties when light is incident on the device.[13] The light, propagating in a single RWG, is diffracted out of the guide. Depending on the wavelengths, this leads to a very high reflection and a low transmission. Two RWGs consisting of two periods $U_1$ and $U_2$ have been demonstrated to achieve color-selective and versatile light steering.[12] The schematic is shown in Figure 1c. Since there are two different periods, the outcoupled mode provides a different direction compared to that of incident light, while sharing the same guided modes inside the waveguide. By changing the period of the second RWG, the 2-RWG scheme filters portions of the spectrum ranges of the white light and redirects them in either the direct reflection or diffraction orders; however, they suffer in lower

**Received:** April 18, 2024
**Revised:** July 22, 2024
**Accepted:** July 22, 2024
**Published:** July 24, 2024

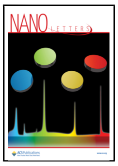

https://doi.org/10.1021/acs.nanolett.4c01858

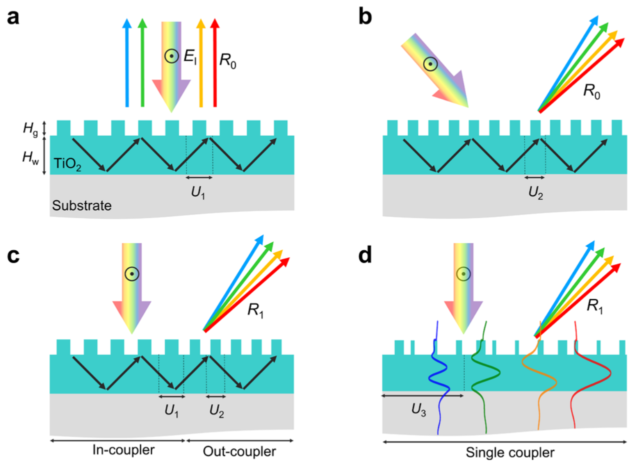

**Figure 1.** (a) Schematic of the normal diffracting RWG with a period of $U_1$. (b) Schematic of the obliquely diffracting RWG with a period of $U_2$. (c) Schematic of RWGs composed of in-coupler and out-coupler working in the visible spectrum. (d) Schematic of MRWG composed of single coupler working for both in- and out-coupling designed by using topology optimization.

efficiency in the specific diffraction order. This challenge can potentially be addressed through inverse design, which starts with desired functionalities and optimizes geometries employing computational algorithms.[19,20] Recent demonstrations of inverse design strategies of metasurface design include topology optimization,[21−24] gradient based inverse design,[25] genetic-type tree optimization,[26] evolutionary optimization,[27] deep learning,[28,29] and hybrid combinations of these approaches. These techniques predominantly target enhancements in local metasurface characteristics. While deep learning can account for global features, it requires large data sets for construction. Although small-data learning[29] methods operate with fewer data points, they still need highly characteristic data (nearly 20). Generating high-characteristic nanostructures corresponding to the spectral data is extremely challenging. In comparison, topology optimization does not require a pre-existing data set, as it optimizes based on gradient characteristics, making it more suitable. Such innovations underscore the transformative potential of inverse design in shaping high-$Q$ and nonlocal metasurfaces, paving the way for diverse applications.

In this study, we experimentally demonstrate a metasurface resonant waveguide grating (MRWG, as depicted in Figure 1d) characterized by outstanding color selectivity and redirection capabilities, along with high $Q$-factors that surpass traditional RWGs. Utilizing an adjoint-based topology optimization method, we incorporate various optimization strategies into the grating structure, resulting in superior performance. This method overcomes the limitations of conventional designs, eliminating the need for specific coupling regions and enabling full-area input and output coupling. This significantly enhances system flexibility and increases the cross-sectional area for more interactions, leading to higher diffraction efficiency and a superior $Q$-factor. Leveraging topological optimization allows us to optimize the grating structure while considering nonlocal effects, providing comprehensive control of light behavior and precise optical functionalities. With appropriate topological optimization strategies, our MRWG design demonstrates advantages in efficient color filtering and high $Q$-factors, making it suitable for applications such as biosensors, near-eye displays, and augmented reality, among others.

In the design process, the essential physics behind optimizations is necessary and helpful for progressing to the inverse design. First, we conducted simulations on two distinct types of RWGs: one with a period of $U_1$ for normal incidence RWG (Figure 1a) and the other with a period of $U_2$ for oblique incidence RWG (Figure 1b). During these simulations, we utilized variables such as $U_1$, $U_2$, waveguide height ($H_w$ = 405 nm), and grating height ($H_g$ = 160 nm) to ensure the overlap of their reflection spectra at resonance wavelengths (see Supporting Information S1). This strategy facilitates selective wavelength filtering, inducing narrow-band resonance effects. We chose to use the same $H_w$ and $H_g$ for both structures because it analogously aligns with the design approach in the literature (Figure 1c).[12] These two structures can be fabricated together, and the two different gratings can share the same guided mode resonances (GMRs).

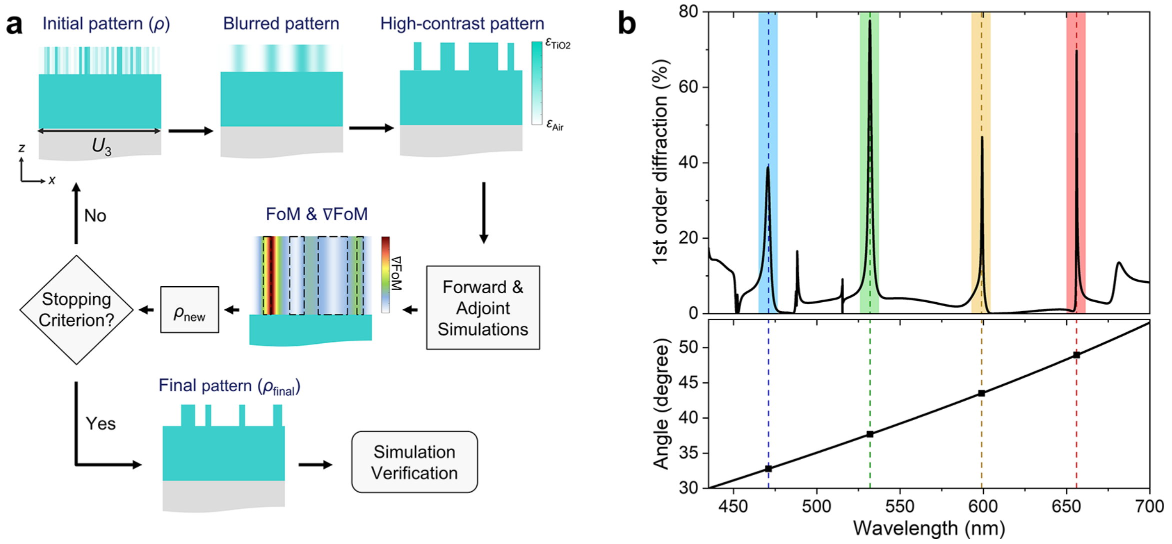

**Figure 2.** (a) Flowchart of the iterative optimization process. (b) Simulated first-order diffraction efficiency and angles of the MRWG. Colored regions represent the operational wavelengths for the four colors at $\lambda_1$ = 471 nm, $\lambda_2$ = 532 nm, $\lambda_3$ = 599 nm, and $\lambda_4$ = 656 nm.

To enhance the diffraction efficiency, we follow the RWG structure illustrated in the forward method (Figure 1c), allocating half of the area to $U_1$ and the remaining half to $U_2$. However, the reported efficiency in the literature has remained below 10%.[12] Therefore, to achieve higher efficiency, we utilize topology optimization (Figure 1d), allowing the entire area to contribute to both input and output coupling. In the meantime, the free-form structure is optimized to enhance diffraction efficiency at desired wavelengths.

The inverse design adopts the topology optimization method, where we initially calculated that the ideal grating period is designed as 870 nm ($U_3$), which is an integer multiple of $U_1$ and $U_2$, generating only first-order diffraction in the visible spectrum. The physics behind this will be discussed in Figure 3b. Subsequently, we employed an adjoint-based topology optimization method for the grating, as illustrated in Figure 2a. We began with a random material distribution $\rho(x)$ as pattern, which continuously varies from 0 to 1, linearly corresponding to relative permittivity values ranging from $\varepsilon_{\mathrm{Air}}$ to $\varepsilon_{\mathrm{TiO2}}$. Subsequently, we utilized the open source rigorous coupled-wave analysis (RCWA) package to perform the electromagnetic simulation of the grating,[30] by setting parameters such as the angle of incidence, mode type, refractive index distribution of each layer, and geometric parameters of the structure. In a forward simulation, we calculated values including diffraction efficiency, the first-order complex amplitude, and forward electric field distribution at the grating. The first-order diffraction efficiency at a wavelength of 532 nm serves as the Figure of Merit (FoM) for this optimization. We then executed a backward simulation to reverse compute the adjoint electric field, using the phase of incidence determined by the first-order complex amplitude from the forward simulation. By utilizing both forward and adjoint electromagnetic simulations, we calculated the FoM gradient at each pixel of the MRWG: that is, ∇FoM. This gradient identifies perturbations in the pattern at pixel locations ($\rho(x)$) that enhance the overall FoM (see Supporting Information S2).

The final step involves iteratively updating the pattern $\rho^{(q+1)}(x)$ with the FoM ($\rho^{(q)}$) and its ∇FoM, where $q$ indicates the $q$th iteration. Constraints are added to the optimization process to ensure that the final pattern converges to a binary design with only two relative permittivity values, $\varepsilon_{\mathrm{Air}}$ and $\varepsilon_{\mathrm{TiO2}}$.[21−23] Initially, the values of pattern $\rho$ range between 0 and 1. As the optimization iterations progress, these values tend to approach 0 or 1. This convergence can be achieved through a contrast function. Low contrast allows for greater freedom in the optimization process, but it may result in the final pattern not approaching values of 0 or 1, leading to mismatched binary patterns and low efficiency. Conversely, high contrast in the final pattern, with values approaching 0 or 1, can approximate a binary pattern, but it may also lead to a more difficult optimization process due to reduced freedom. Additionally, we consider the fabrication feasibility of the structure, which can be addressed by using a blur function with a specific radius. We determine a suitable blur radius to be 28 nm, corresponding to a blur dimension or line width of approximately 54 nm, matching our fabrication limitations. The aspect ratio of the meta-atoms reaches about 3, which is smaller than the typical aspect ratio of nanopillars, ranging from 5 to 8. A larger blur radius reduces the geometric freedom and the potential for higher efficiency, whereas a smaller radius results in more complex fabrication processes.

We validated the optimized MRWG by examining the simulation results. The diffraction efficiency is depicted in Figure 2b. The incident light is illuminated normally, covering a range of visible wavelengths. It is observed that peak values occur at wavelengths of 471, 532, 599, and 656 nm, respectively. This indicates that the MRWG successfully reflects blue, green, yellow, and red light within the visible spectrum. The full width at half-maximum (fwhm) of the four peaks ranges from 0.48 to 3.59 nm. Our MRWG, designed with topology optimization, significantly increases efficiency, reaching up to 77.7% (for additional analyses, refer to Supporting Information S3−S6). Without using topology optimization, the efficiency reported in the literature is less than 10%.[12] Furthermore, the $Q$-factor is determined by the guided modes, and our results show very high $Q$-factors ranging from 131 to 1367; detailed values are presented in Table 1.

**Table 1. Simulation Numerical Statistics**

| | wavelength (nm) | efficiency (%) | fwhm (nm) | Q-factor | diffraction angle (deg) |
|---|---|---|---|---|---|
| $\lambda_1$ | 471 | 38.8 | 3.59 | 131 | 32.8 |
| $\lambda_2$ | 532 | 77.7 | 2.25 | 236 | 37.7 |
| $\lambda_3$ | 599 | 46.8 | 0.952 | 630 | 43.6 |
| $\lambda_4$ | 656 | 69.7 | 0.482 | 1362 | 49.0 |

We employed a momentum analysis approach to investigate the resonance wavelength phenomenon in the MRWG structure. To begin, we take the resonance at red light ($\lambda_4$) for example, with the physical phenomena extendable to other wavelengths. The transverse momentum of light coupling into the waveguide can be obtained by the momentum conservation equation for in-coupling (eq 1), which is

$$k\sin\theta_{\mathrm{in}} + m_{\mathrm{in}}G = \beta_n \qquad (1)$$

Here, $k$ represents the wavenumber, $\beta_n$ is the transverse momentum, $\theta_{\mathrm{in}}$ is the angle of incidence, and $G$ denotes the grating momentum, which is $2\pi/U_3$. When light is normal incident to the MRWG, the transverse momentum from the light is zero. The momentum coupled inside the waveguide is then determined by $G$ with $m_{\mathrm{in}}$ times.

Additionally, the $\beta_n$ of light coupling out from the waveguide can be obtained through the momentum conservation equation for out-coupling (eq 2), which is

$$\beta_n + m_{\mathrm{out}}G = k\sin\theta_{\mathrm{out}} \qquad (2)$$

The diffraction angle $\theta_{\mathrm{out}}$ is then estimated, where the momentum $k\sin\theta_{\mathrm{out}}$ is influenced by adding $\beta_n$ with $m_{\mathrm{out}}$ times $G$. Figure 3a,b visualizes the momentum conservation process described above. The values of ($m_{\mathrm{in}}$, $m_{\mathrm{out}}$) are (−3, 4), where a negative value indicates a negative direction or momentum as the guided mode propagates inside the waveguide ($\beta_n = -3G$). In Figure 3b, it can be observed that the $-3G$ momentum corresponds to a specific mode number ($n$th) at wavelengths ranging from $\lambda_4$ to $\lambda_1$. Similarly, when coupling out of the waveguide, the light experiences a $4G$ momentum into the air layer, leading to a positive diffraction angle ($\theta_{\mathrm{out}}$) as determined by eq 2. This structure also provides the possibility values of ($m_{\mathrm{in}}$, $m_{\mathrm{out}}$) as (4, −3), but with much lower efficiency, e.g., resonances at 452, 488, and 515 nm as shown in Figure 2b. This case has $4G$ momentum propagating inside the waveguide (details in Supporting Information S3).

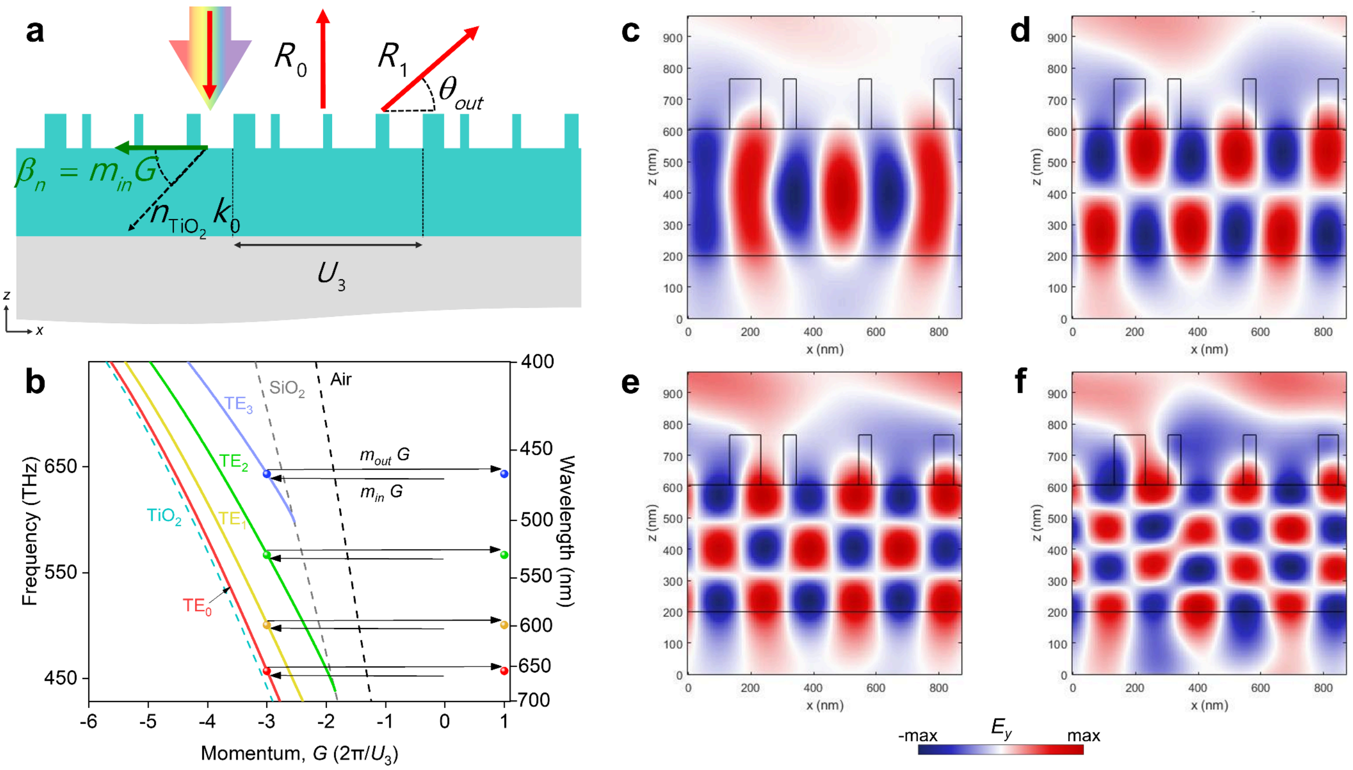

**Figure 3.** (a) Schematic representation of the momentum relationship when light is incident on the MRWG with a $U_3$ period. (b) Modal relation for the waveguide modes supported by the $TiO_2$ waveguide. The black, gray, and cyan dashed curves are the light lines for Air, $SiO_2$ and $TiO_2$, respectively. The horizontal arrow to the left indicates the excitation of the grating by a normally incident planewave. The arrow to the right designates the decoupling from the $TE_n$ waveguide mode into the first diffracted order. $U_3$ is the grating period. (c−f) Electric field ($E_y$) of waveguide resonance effects: (c) fundamental mode ($TE_0$) at a wavelength of 656 nm; (d) second mode ($TE_1$) at a wavelength of 599 nm; (e) third ($TE_2$) mode at a wavelength of 532 nm; (f) fourth mode ($TE_3$) at a wavelength of 470 nm.

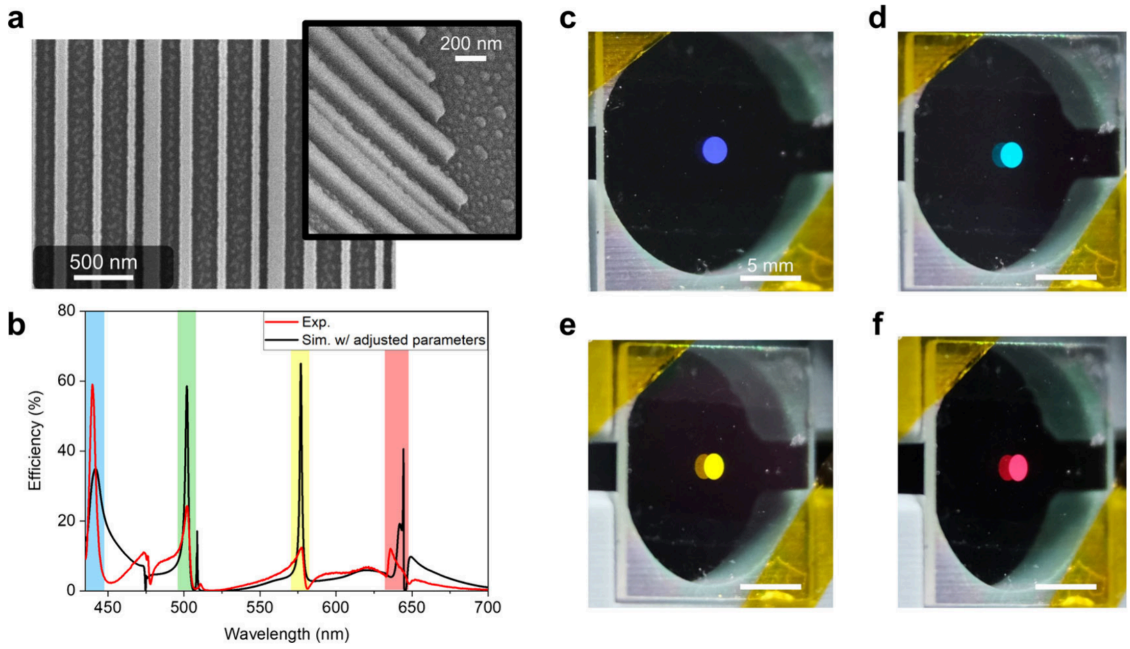

**Figure 4.** (a) SEM image displaying the MRWG sample, with an inset showing the 45° tiled view of a portion of the sample. (b) Comparison of measured spectrum of MRWG (red line) and simulated spectrum with adjusted parameters (black line). Colored regions highlight the good alignment of peak wavelengths. (c−f) MRWG reflection images captured using a microfocus camera.

The significance of values 3 and 4 is linked to the relationship of $3U_1 = 4U_2$. In other words, initially, $U_3 = |m_{in}|U_1 = |m_{out}|U_2$. Therefore, the design principle of the MRWG, such as momentum conservation while coupling in and out of the structure, is determined by the coupling momentum coefficients ($m_{in}$, $m_{out}$).

Ultimately, we utilized Figure 3b to identify the resonance wavelengths corresponding to the mode number ($n$th) when $\beta_n = -3G$. This process resulted in obtaining cross-sectional images of four resonance mode numbers from Figure 3c−f. The electric field exhibits 0 (1, 2, 3) node(s) along the $z$-direction, corresponding to the $TE_0$ ($TE_1$, $TE_2$, $TE_3$) waveguide modes. In other words, $\beta_1$−$\beta_4$ at $\lambda_4$−$\lambda_1$ correspond to quantized waveguide modes.

We fabricated our MRWG sample using electron-beam lithography, atomic layer deposition, and the high-density plasma reactive ion etching (HDP-RIE) method (see Supporting Information S7 for detailed manufacturing procedures). Figure 4a shows the scanning electron microscope (SEM) image of our fabricated sample, which includes ~3 periods with a structure distribution consistent with the MRWG. The tiled SEM image shown in the inset of Figure 4a indicates a grating height of about 160 nm. Subsequently, we conducted spectral measurements of the first-order reflective diffraction efficiency as a function of wavelength using our experimental setup (see Supporting Information S8 for details), as depicted in Figure 4b. In this spectrum, red lines represent the experimental results. Four distinct peaks can be observed. It is worth noting that the efficiency is particularly high (59.1%) in the blue spectral region, with a relatively high $Q$-factor as high as 93.2. Detailed experimental values of the MRWG are presented in Supporting Information Table S1.

However, we observe a blue shift in the experimentally measured peaks compared to the optimization results along with relatively lower efficiency. After investigating structural and refractive index inaccuracies, we found that this result could be attributed to process inaccuracies and $TiO_2$ refractive index discrepancies (see Supporting Information S8). These factors led to a lower efficiency and a blue shifting of the peaks. Figure 4b shows a good alignment of peak wavelengths in the simulated spectrum with adjusted parameters (black line) and in the experimental spectrum (red line). The simulated spectrum indicates a lower refractive index for $TiO_2$ and overetched waveguides in the experiments.

Figure 4c−f displays images of the MRWG captured using a microfocus camera. We positioned the camera at specific angles corresponding to the 4 diffraction peaks and captured images accordingly. This process required precise alignment of the camera at specific angles to observe and capture optical effects. In these captured images, from left to right, we have the reflection effects in different colors for blue, cyan (blue shift of green), yellow, and red light. Different colors represent the diffraction peak of MRWG at 4 designed wavelengths, and these effects are only visible at specific angles, further illustrating the color-selective properties of the MRWG.

In this study, we experimentally demonstrate a novel MRWG that utilizes adjoint-based topology optimization to achieve remarkable color selectivity, redirection capabilities, and high $Q$-factors. Effectively overcoming the limitations of traditional RWGs, such as specific coupling regions, our MRWG design provides a full area for both input and output coupling, increasing flexibility and interaction area for enhanced overall efficiency and $Q$-factors. Incorporating nonlocal effects into the topology optimization process enables precise control of the light behavior, allowing efficient color filtering and high $Q$-factors. The MRWG design successfully diffracts blue, green, yellow, and red light beams with peak efficiency, as observed in experimental results. Despite minor discrepancies between experimental and simulation results due to process inaccuracies and unsatisfactory refractive index, the MRWG's color-selective properties are clearly demonstrated, offering promising opportunities for various optical applications. In summary, the MRWG design presented in this study represents a significant advancement in metasurface technology, showcasing its potential for practical and efficient color selectivity and redirection. Additionally, for one-dimensional optimization, the FoM was set for a single wavelength, resulting in 4 high-$Q$ wavelengths being optimized simultaneously. This occurs because the low degrees of freedom in 1D optimization tend to couple out resonance wavelength. In the future, if there is a need to depress a specific wavelength or select only one wavelength, more structural freedom, such as 2D optimization, will be necessary. Our MRWG is suitable for a wide range of applications, including biosensors,[31] genetic screening,[32] near-eye displays,[33] and augmented reality.[34,35] This research contributes to the ongoing development of metasurfaces with improved performance in spectrum engineering and diverse applications in narrow-band nanophotonics.

## ASSOCIATED CONTENT

### Supporting Information

The Supporting Information is available free of charge at https://pubs.acs.org/doi/10.1021/acs.nanolett.4c01858.

> Additional details of initial forward design, iterative optimization process, simulations of different incidence in TE and TM modes, fabrication process, optical setup, and experimental results (PDF)

## AUTHOR INFORMATION

### Corresponding Author

**Yao-Wei Huang** − *Department of Photonics, College of Electrical and Computer Engineering, National Yang Ming Chiao Tung University, Hsinchu 300093, Taiwan;* orcid.org/0000-0001-8983-413X; Email: ywh@nycu.edu.tw

### Authors

**Huan-Teng Su** − *Department of Photonics, College of Electrical and Computer Engineering, National Yang Ming Chiao Tung University, Hsinchu 300093, Taiwan*

**Lu-Yun Wang** − *Department of Photonics, College of Electrical and Computer Engineering, National Yang Ming Chiao Tung University, Hsinchu 300093, Taiwan*

**Chih-Yao Hsu** − *Department of Photonics, College of Electrical and Computer Engineering, National Yang Ming Chiao Tung University, Hsinchu 300093, Taiwan*

**Yun-Chien Wu** − *Department of Photonics, College of Electrical and Computer Engineering, National Yang Ming Chiao Tung University, Hsinchu 300093, Taiwan*

**Chang-Yi Lin** − *Department of Photonics, College of Electrical and Computer Engineering, National Yang Ming Chiao Tung University, Hsinchu 300093, Taiwan*

**Shu-Ming Chang** − *Department of Photonics, College of Electrical and Computer Engineering, National Yang Ming Chiao Tung University, Hsinchu 300093, Taiwan*

Complete contact information is available at: https://pubs.acs.org/10.1021/acs.nanolett.4c01858

### Author Contributions

Y.-W.H. initiated the study and contributed required materials and analysis tools. Y.-W.H., L.-Y.W., and H.-T.S. performed the numerical calculation, topology optimization, and simulation. L.-Y.W., H.-T.S., Y.-C.W., C.-Y.L., and S.-M.C. fabricated metasurface samples. H.-T.S., C.-Y.H., and L.-Y.W. performed the optical experiments. H.-T.S. and Y.-W.H. analyzed experimental data and wrote the manuscript. All authors discussed the results and commented on the manuscript.

### Funding

National Science and Technology Council in Taiwan (Grant Nos. 110−2112-M-A49-034-MY3 and 113-2112-M-A49-025).

### Notes

The authors declare no competing financial interest.

## ■ ACKNOWLEDGMENTS

This work was supported by the National Science and Technology Council in Taiwan and the Ministry of Education in Taiwan under the Yushan Young Scholar Program. This work was performed in part at the Nano Facility Center (NFC) in NYCU, the Center for Nano Science and Technology (CNST) in NYCU, and Taiwan Semiconductor Research Institute (TSRI). We also extend our gratitude to Prof. Federico Capasso and Leonardo DRS for their support during the initial stages of this study, exploring the possibilities.

## ■ REFERENCES

(1) Overvig, A.; Alù, A. Diffractive Nonlocal Metasurfaces. *Laser Photonics Rev.* **2022**, *16* (8), 2100633.

(2) Shastri, K.; Monticone, F. Nonlocal Flat Optics. *Nat. Photonics* **2023**, *17* (1), 36−47.

(3) Yu, N.; Genevet, P.; Kats, M. A.; Aieta, F.; Tetienne, J.-P.; Capasso, F.; Gaburro, Z. Light Propagation with Phase Discontinuities: Generalized Laws of Reflection and Refraction. *Science* **2011**, *334* (6054), 333−337.

(4) Arbabi, A.; Horie, Y.; Bagheri, M.; Faraon, A. Dielectric Metasurfaces for Complete Control of Phase and Polarization with Subwavelength Spatial Resolution and High Transmission. *Nat. Nanotechnol.* **2015**, *10* (11), 937−943.

(5) Hsu, W.-L.; Chen, Y.-C.; Yeh, S. P.; Zeng, Q.-C.; Huang, Y.-W.; Wang, C.-M. Review of Metasurfaces and Metadevices: Advantages of Different Materials and Fabrications. *Nanomaterials* **2022**, *12* (12), 1973.

(6) Khorasaninejad, M.; Chen, W. T.; Devlin, R. C.; Oh, J.; Zhu, A. Y.; Capasso, F. Metalenses at Visible Wavelengths: Diffraction-Limited Focusing and Subwavelength Resolution Imaging. *Science* **2016**, *352* (6290), 1190−1194.

(7) Huang, Y.-W.; Chen, W. T.; Tsai, W.-Y.; Wu, P. C.; Wang, C.-M.; Sun, G.; Tsai, D. P. Aluminum Plasmonic Multicolor Meta-Hologram. *Nano Lett.* **2015**, *15* (5), 3122−3127.

(8) Balthasar Mueller, J. P.; Rubin, N. A.; Devlin, R. C.; Groever, B.; Capasso, F. Metasurface Polarization Optics: Independent Phase Control of Arbitrary Orthogonal States of Polarization. *Phys. Rev. Lett.* **2017**, *118* (11), 113901.

(9) Overvig, A. C.; Shrestha, S.; Malek, S. C.; Lu, M.; Stein, A.; Zheng, C.; Yu, N. Dielectric Metasurfaces for Complete and Independent Control of the Optical Amplitude and Phase. *Light Sci. Appl.* **2019**, *8* (1), 92.

(10) Sroor, H.; Huang, Y.-W.; Sephton, B.; Naidoo, D.; Vallés, A.; Ginis, V.; Qiu, C.-W.; Ambrosio, A.; Capasso, F.; Forbes, A. High-Purity Orbital Angular Momentum States from a Visible Metasurface Laser. *Nat. Photonics* **2020**, *14* (8), 498−503.

(11) Lemarchand, F.; Sentenac, A.; Cambril, E.; Giovannini, H. Study of the Resonant Behaviour of Waveguide Gratings: Increasing the Angular Tolerance of Guided-Mode Filters. *J. Opt. Pure Appl. Opt.* **1999**, *1* (4), 545−551.

(12) Quaranta, G.; Basset, G.; Martin, O. J. F.; Gallinet, B. Color-Selective and Versatile Light Steering with up-Scalable Subwavelength Planar Optics. *ACS Photonics* **2017**, *4* (5), 1060−1066.

(13) Quaranta, G.; Basset, G.; Martin, O. J. F.; Gallinet, B. Recent Advances in Resonant Waveguide Gratings. *Laser Photonics Rev.* **2018**, *12* (9), 1800017.

(14) Overvig, A. C.; Malek, S. C.; Yu, N. Multifunctional Nonlocal Metasurfaces. *Phys. Rev. Lett.* **2020**, *125* (1), 017402.

(15) Malek, S. C.; Overvig, A. C.; Alù, A.; Yu, N. Multifunctional Resonant Wavefront-Shaping Meta-Optics Based on Multilayer and Multi-Perturbation Nonlocal Metasurfaces. *Light Sci. Appl.* **2022**, *11* (1), 246.

(16) Richter, F. U.; Sinev, I.; Zhou, S.; Leitis, A.; Oh, S.-H.; Tseng, M. L.; Kivshar, Y.; Altug, H. Gradient High-Q Dielectric Metasurfaces for Broadband Sensing and Control of Vibrational Light-Matter Coupling. *Adv. Mater.* **2024**, *36* (25), 2314279.

(17) Lawrence, M.; Barton, D. R.; Dixon, J.; Song, J.-H.; van de Groep, J.; Brongersma, M. L.; Dionne, J. A. High Quality Factor Phase Gradient Metasurfaces. *Nat. Nanotechnol.* **2020**, *15* (11), 956−961.

(18) Klopfer, E.; Dagli, S.; Barton, D. I.; Lawrence, M.; Dionne, J. A. High-Quality-Factor Silicon-on-Lithium Niobate Metasurfaces for Electro-Optically Reconfigurable Wavefront Shaping. *Nano Lett.* **2022**, *22* (4), 1703−1709.

(19) Ma, W.; Liu, Z.; Kudyshev, Z. A.; Boltasseva, A.; Cai, W.; Liu, Y. Deep Learning for the Design of Photonic Structures. *Nat. Photonics* **2021**, *15* (2), 77−90.

(20) Li, Z.; Pestourie, R.; Lin, Z.; Johnson, S. G.; Capasso, F. Empowering Metasurfaces with Inverse Design: Principles and Applications. *ACS Photonics* **2022**, *9* (7), 2178−2192.

(21) Sell, D.; Yang, J.; Doshay, S.; Yang, R.; Fan, J. A. Large-Angle, Multifunctional Metagratings Based on Freeform Multimode Geometries. *Nano Lett.* **2017**, *17* (6), 3752−3757.

(22) Wang, E. W.; Sell, D.; Phan, T.; Fan, J. A. Robust Design of Topology-Optimized Metasurfaces. *Opt. Mater. Express* **2019**, *9* (2), 469−482.

(23) Shi, Z.; Zhu, A. Y.; Li, Z.; Huang, Y.-W.; Chen, W. T.; Qiu, C.-W.; Capasso, F. Continuous Angle-Tunable Birefringence with Freeform Metasurfaces for Arbitrary Polarization Conversion. *Sci. Adv.* **2020**, *6* (23), No. eaba3367.

(24) Xu, M.; Pu, M.; Sang, D.; Zheng, Y.; Li, X.; Ma, X.; Guo, Y.; Zhang, R.; Luo, X. Topology-Optimized Catenary-like Metasurface for Wide-Angle and High-Efficiency Deflection: From a Discrete to Continuous Geometric Phase. *Opt. Express* **2021**, *29* (7), 10181.

(25) Li, Z.; Pestourie, R.; Park, J.-S.; Huang, Y.-W.; Johnson, S. G.; Capasso, F. Inverse Design Enables Large-Scale High-Performance Meta-Optics Reshaping Virtual Reality. *Nat. Commun.* **2022**, *13* (1), 2409.

(26) Lin, C.-H.; Chen, Y.-S.; Lin, J.-T.; Wu, H. C.; Kuo, H.-T.; Lin, C.-F.; Chen, P.; Wu, P. C. Automatic Inverse Design of High-Performance Beam-Steering Metasurfaces via Genetic-Type Tree Optimization. *Nano Lett.* **2021**, *21* (12), 4981−4989.

(27) Zhu, D. Z.; Whiting, E. B.; Campbell, S. D.; Burckel, D. B.; Werner, D. H. Optimal High Efficiency 3D Plasmonic Metasurface Elements Revealed by Lazy Ants. *ACS Photonics* **2019**, *6* (11), 2741−2748.

(28) Ueno, A.; Lin, H.-I.; Yang, F.; An, S.; Martin-Monier, L.; Shalaginov, M. Y.; Gu, T.; Hu, J. Dual-Band Optical Collimator Based on Deep-Learning Designed, Fabrication-Friendly Metasurfaces. *Nanophotonics* **2023**, *12* (17), 3491−3499.

(29) Lin, C.-H.; Huang, S.-H.; Lin, T.-H.; Wu, P. C. Metasurface-Empowered Snapshot Hyperspectral Imaging with Convex/Deep (CODE) Small-Data Learning Theory. *Nat. Commun.* **2023**, *14* (1), 6979.

(30) Hugonin, J. P.; Lalanne, P. RETICOLO Software for Grating Analysis. arXiv January 8, 2023. DOI: 10.48550/arXiv.2101.00901.

(31) Daghestani, H. N.; Day, B. W. Theory and Applications of Surface Plasmon Resonance, Resonant Mirror, Resonant Waveguide

Grating, and Dual Polarization Interferometry Biosensors. *Sensors* **2010**, *10* (11), 9630−9646.

(32) Hu, J.; Safir, F.; Chang, K.; Dagli, S.; Balch, H. B.; Abendroth, J. M.; Dixon, J.; Moradifar, P.; Dolia, V.; Sahoo, M. K.; Pinsky, B. A.; Jeffrey, S. S.; Lawrence, M.; Dionne, J. A. Rapid Genetic Screening with High Quality Factor Metasurfaces. *Nat. Commun.* **2023**, *14* (1), 4486.

(33) Kress, B.; Starner, T.; Kazemi, A. A.; Kress, B. C.; Thibault, S. A Review of Head-Mounted Displays (HMD) Technologies and Applications for Consumer Electronics. *SPIE Proc.* **2013**, 87200A.

(34) Huang, T.-W.; Chung, Y.-C.; Lai, Y.-C.; Sung, Y.-H.; Hsu, Y.-S.; Hung, W.-C.; Huang, C.-Y.; Cheng, Y.-C. Metagrating-Based Augmented Reality near-Eye Display. In *Optical Architectures for Displays and Sensing in Augmented, Virtual, and Mixed Reality (AR, VR, MR) II*; SPIE: 2021; Vol. *11765*, pp 71−76. DOI: 10.1117/12.2580023.

(35) Drazic, V.; Shramkova, O.; Varghese, B.; Blondé, L.; De La Perrière, V. B.; Schiffler, J.; Twardowski, P.; Lecler, S.; Walter, B.; Mairiaux, E.; Bavedila, F.; Faucher, M.; Allié, V. Over-Wavelength Pitch Sized Diffraction Gratings for Augmented Reality Applications. *Opt. Express* **2022**, *30* (2), 1293.